Structure and activity of supported bimetallic NiPd nanoparticles: influence of preparation method on CO2 reduction

Adriano H Braga, Natália J S Costa, Karine Philippot, Renato V Gonçalves, János Szanyi, Liane Marcia Rossi

DOI: 10.1002/ ((please add manuscript number))
Article type: Full Paper

Structure and activity of supported bimetallic NiPd nanoparticles: influence of preparation method on CO_2 reduction

*Adriano H. Braga, Natália J. S. Costa, Karine Phillipot, Renato V. Gonçalves, János Szanyi, Liane M. Rossi**

Dr. Adriano H. Braga, Dr. Natália J. S. Costa, Prof. Liane M. Rossi
Department of Fundamental Chemistry, Institute of Chemistry, University of São Paulo
Av. Lineu Prestes, 748, São Paulo, SP, 05508-000, Brazil
E-mail: lrossi@iq.usp.br
Dr. Karine Phillipot
CNRS, LCC (Laboratoire de Chimie de Coordination), Université de Toulouse;
205, route de Narbonne, F-31077 Toulouse cedex 4, France
Prof. Renato V. Gonçalves
São Carlos Institute of Physics, University of São Paulo,
13560-970, São Carlos, SP, Brazil
Dr. János Szanyi
Institute for Integrated Catalysis, Pacific Northwest National Laboratory,
Richland, WA, 99352, United States

Keywords: bimetallic, CO_2, segregation, alloy, activity

Bimetallic Ni-Pd and Ni, Pd reference catalysts were prepared by decomposing organometallic precursors, $Ni(cod)_2$ and $Pd_2(dba)_3$, leading to nanoparticles with sizes ranging from 3 to 6 nm. Two different synthesis procedures were followed: i) solution synthesis using capping ligand (hexadecylamine) followed by impregnation of pre-formed nanoparticles on SiO_2, called Sol-immobilization (SI); and 2) direct precursor decomposition onto SiO_2, without stabilizer, called Direct Decomposition (DD). Samples prepared by SI procedure are alloyed bimetallic nanoparticles, whereas samples obtained by DD one show phase segregation. Interestingly, DD samples show better activity for CO_2 hydrogenation into CO (reverse water-gas shift reaction - RWGS), than SI ones. The 1Ni:1Pd DD sample, that has the lowest activation energy for RWGS, shows high concentration of surface undercoordinated sites. These sites chemisorb CO weakly, thus improving activity in RWGS,

in opposition to other samples that chemisorb CO strongly, in multibond configuration, having lower activity and selectivity. The results indicate that different decomposition rates drive the formation of smaller and more active Ni clusters, when in presence of Pd. However, the knowledge acquired here on the influence of synthesis conditions on the catalytic properties of Ni-Pd catalysts should help in finding better catalysts for CO_2 transformation.

1. Introduction

Carbon dioxide, generated in several industrial chemical processes is a greenhouse gas which made the scientific community to boost efforts in its recycling using catalytic chemical processes, in order to produce value-added chemicals. The reverse water-gas shift (RWGS) reaction converts CO_2 into CO (ΔH^0=41 kJ mol^{-1}) and is among the possible ways to reuse CO_2 by means of an integrated RWGS/Fischer-Tropsch synthesis. One main drawback of RWGS is the selectivity towards CO at low temperature, since the hydrogenation of CO_2 to CH_4 is a thermodynamically favorable side-reaction (ΔH^0=-164 kJ mol^{-1}). In principle, RWGS reaction can be seen as intermediary step to the methanation process, since the CO formed can be hydrogenated to methane,[1] and also for other hydrocarbon processing like oxidative dehydrogenation of alkanes[2] and reforming reactions.[3,4] RWGS is also an important model reaction to study structure and activity correlations. The H_2/CO_2 molar ratio and the metal particle size in the catalysts are mostly reported as factors that influence the catalytic selectivity in RWGS.[5,6] A high H_2 concentration is known to enhance the hydrogenation to methane.[7] Small nanoclusters generally improve the selectivity to CO,[6] which might be due to the higher density of low-coordinated atoms on top of small nanoclusters,[8] while larger particles size and high metal loadings have been associated to CH_4 production,[9,10] although there is still discussion about the particle size effects on pathways of CO_2 reduction reactions.[11]

Nickel is a classical hydrogenation catalyst that is typically used for the hydrogenation of CO_2 to methane.[12,13] This metal is of interest due to its relatively low-price, high abundance and elevated activity.[14,15] It is believed that a support-metal interaction can influence CO_2 activation.[16,17] H_2 dissociation occurs on Ni surface, which provides H atoms able to reduce CO_2 to CO or directly to CH_4, or also the hydrogenation of the formed CO to CH_4. The reaction pathways depend strongly on the structure of Ni sites. But Ni usually suffers deactivation with time on stream due to sintering, coke formation, and sometimes oxidation. Bimetallic compounds are a frequently used strategy to improve stability and selectivity.[18] Pd, like Ni, is a metal that can easily dissociate H_2, and is also known as a catalyst for hydrocarbon transformation and oxidation reactions.[8,19,20] However, the high cost of Pd prohibits its large-scale use as a promoter, in favor to more abundant and low-cost metals. Theoretical calculations on different metal surfaces demonstrated that Ni has a d-band center energy closer to the Fermi level than Pd;[21–23] also the O binding energy on Ni is higher than on Pd, and the activation barrier for O bonding to the metal surface is lower on Ni compared to Pd.[8] In terms of CO chemisorption energy, Ni values (BE_{CO}= 2.17 eV) are slightly higher than Pd (BE_{CO}= 2.36 eV).[8,22] Hence, Ni appears to be more reactive towards *CO, *O and *H, and more oxophilic than Pd. The alloying of Pd with Ni has a lower effect on disturbing Pd electronic properties, but the addition of Pd to Ni surfaces could slightly decrease the reactivity of Ni, thus decreasing the CO bonding energy to the catalyst surface. This, in turn, can help CO desorption to gas phase. Additionally, except for tetrahedron and cubic shaped nanoparticles, NiPd nanoalloys are found to be relatively stable in a broad range of compositions.[24]

The organometallic complex $Ni(cod)_2$ has been described as a good precursor to Ni clusters,[25,26] being easily decomposed under H_2 atmosphere at low temperature that leads to well-defined particle size distribution and existence of Ni(0) species if caution is taken.[27] The direct preparation of Ni^0 avoids an additional thermal procedure usually necessary to

reduce Ni^{2+} species to metallic state.[28] We previously reported the direct deposition of Ni^0 nanoparticles (Ni NPs) by the *in-situ* decomposition of the organometallic precursor $Ni(cod)_2$ over silica-coated magnetite nanoparticles,[25] which resulted in a very active nickel catalyst for hydrogenation of cyclohexene under mild conditions. On the contrary, sol-immobilization of pre-formed Ni NPs prepared by decomposition of $Ni(cod)_2$ in hexadecylamine media produced poorly active Ni catalyst. The organometallic complex $Pd_2(dba)_3$ is also known as a good precursor for Pd NPs, being also easily decomposed in mild reaction conditions.[26] Interestingly, we have also reported the controlled synthesis of well-defined Pd and Ni_xPd_y NPs using hexadecylamine (HDA) as a stabilizer, which were successfully deposited onto silica-coated Fe_3O_4 nanoparticles[26] by the sol–immobilization method for application in hydrogenation catalysis. In this previous work, excess HDA was removed during a post-impregnation washing step with pentane, but HDA was still present at the metal surface. To avoid the interference of HDA, in the present work we are investigating the synthesis of NiPd NPs by direct co-decomposition of parent organometallic precursors over the support without adding a stabilizer.

Herein, the advantages of using $Ni(cod)_2$ and $Pd_2(dba)_3$ organometallic complexes were explored for the synthesis of well-defined Ni and NiPd NPs. Different Ni:Pd molar ratios have been applied in order to modify the electronic structure of Ni in a controlled way and to investigate the composition/structure effect on RWGS. Colloidal NiPd NPs were synthesized using HDA as a stabilizer and then deposited onto a support by taking advantage of our previous knowledge to achieve well-defined alloyed bimetallic systems, in order to rationalize the effect of Ni/Pd composition on RWGS. Also, in order to obtain more realistic catalysts, a direct co-decomposition of the two organometallic precursors over the support was performed without capping ligand. To accurately study the compositional and size effects, SiO_2 nanospheres were used as a support. These catalysts were evaluated in RWGS reaction

at low H_2 partial pressure in order to limit the CH_4 formation, by decreasing the equilibrium constant for the hydrogenation reaction pathway.

2. Results and Discussion

2.1. Metal composition, particle size distribution and NiPd configuration in bimetallic catalysts

The metal content and the bulk Pd concentration, determined by ICP-OES, and the surface Pd concentration, determined by XPS, for the two series of catalysts are summarized in **Table 1**. The catalysts prepared by the direct decomposition of organometallic precursors on functionalized silica support (DD) present a concentration of NiPd metal at least 4 times larger compared with preformed colloidal nanoparticles on the same support. The presence of capping ligand (hexadecylamine, HDA) with long carbonic chain may explain this difference, as the result of a steric hindrance around the NPs that limits their incorporation onto the amino-functionalized silica support.[26] The bulk and surface Pd molar fractions calculated from experimental results (ICP-OES and XPS) were found to be close to the nominal values. These results suggest that the Ni and Pd elements are well-distributed in the catalysts; however, the characterization of bimetallic nanoparticles is a difficult task owing to different possible structures, such as core–shell, ordered or disordered alloys, or even segregated phases. More information was obtained by morphological analysis (*vide infra*).

In order to compare the two preparation methods, a structural analysis of the Ni, Pd and NiPd catalysts was done. The characterization of the catalysts prepared by sol-immobilized method (SI) was reported in a previous work.[26] The TEM images of the catalysts prepared by the direct decomposition method (DD) are shown in Supplementary Information (**Figure S1**) and the histograms of particle size distributions are given in the (**Figure S2**). With mean sizes in the range of 3.2 to 4.2 nm, the nanoparticle sizes of DD

samples are quite lower than those for SI samples where mean sizes in the range of 4.2 to 6.3 nm were observed. However, size distributions are comparable for both methodologies.

A comparison of elemental content, morphology and structure in supported catalysts prepared by DD and SI methodologies was investigated by high-resolution STEM with EDS elemental mapping for the representative NiPd (1:1 molar ratio) (**Figure 1**). The results for Ni_5Pd_5 DD catalyst (Figure 1a-d**)** show segregation of small Ni clusters and larger Pd NPs. Metal segregation usually derive from the different decomposition kinetics of $Ni(cod)_2$ and $Pd_2(dba)_3$ precursors, which may induce a successive metal deposition on the support instead of allowing the kinetic control necessary for alloy formation. In contrast, for the SI samples, the mapping results (Figure 1e-h) revealed homogeneous metal distribution attesting of the formation of alloyed nanoparticles. This can be explained by the better conditions offered by the solution synthesis method applied for elaborating the SI catalysts.

X-ray diffraction patterns were recorded for NiPd DD samples (**Figure S3**). Due to their low metal content, no XRD peaks were detected for SI samples. The obtained XRD patterns for NiPd DD catalysts show an amorphous halo from SiO_2 and diffraction peaks assigned to the Fe_3O_4 core, at ca. 30.5, 35.5, 43.4, 54.0, 57.4 and 63.0^o mainly. Additional peaks can be attributed to metallic Ni (ca. 44.5° at Ni DD) and metallic Pd (ca. 40.2° and 47.1° at Pd DD). The Ni_5Pd_5 DD sample did not show reflections that could be attributed to pure Ni, but this can be expected if very small clusters have been obtained. Also, the Pd XRD peaks did not show any shift to higher 2θ values as can be expected when alloying with Ni.[29] These results are in agreement with the STEM/EDS analysis showing very small Ni clusters segregated from Pd nanoparticles (Figure 2b-d).

2.2. CO_2 activation and conversion through RWGS

After reduction treatment at 400 °C for 30 min, the catalysts were tested in the hydrogenation of CO_2 reaction using 1:1 (CO_2:H_2) gas composition in a temperature range from 150 to 700

ºC. The curves of conversion obtained as function of temperature for all Ni_xPd_y catalysts are shown in **Figure 2**. CO_2 conversion starts at about 250 °C for the sample of pure Ni whatever the preparation method. Pure Pd catalysts (Pd DD) sample showed an onset temperature for CO_2 conversion at around 450 °C and at temperatures higher than 600 °C for the Pd SI sample. The addition of Pd to Ni shifts the CO_2 conversion to higher temperatures for the SI samples (Figure 3b). Among the DD samples, the Ni_5Pd_5 DD starts the reaction at the same temperature as pure Ni_1 DD while the Ni_1Pd_9 DD sample becomes active at ca. 350 °C (Figure 3a). Regarding the selectivity, the CO and CH_4 formation rates as function of temperature are shown in **Figure 3**. All the samples displayed low formation of methane (quantities in the range of 2% in molar fraction at the reactor outlet) but that of CO as the main product, thus showing a high selectivity towards RWGS. The overall rate of methane formation is given in **Table 2** for all catalysts.

Pure Ni and Ni-rich samples presented higher methane formation rates, with Ni SI sample showing the highest rate of CH_4 formation at 400 ºC (Figure 3d). Interestingly, for DD samples, the methane formation was almost the same for Ni DD and Ni_5Pd_5 DD (Figure 3c). The temperature of maximum methane formation follows well the conversion curves, i.e. the methane starting to be formed when CO_2 starts to be converted. Ni_1 DD and Ni_5Pd_5 DD catalysts showed a maximum methane formation temperature of 450°C, whereas for Ni_1Pd_9 DD and Pd DD it was 550°C. For the SI samples, the rate of methane formation decreased at higher Pd loading, being Pd SI the sample that yielded the lowest amount of CH_4 (Figure 3d). Regarding the temperatures for maximum CH_4 formation, it was at 400 °C for Ni SI, and 550 °C for the Ni_5Pd_5, Ni_9Pd_1 and Pd_1 SI samples.

The apparent activation energy (E_a^{app}; Table 2) was estimated at conversion rates lower than 25% from Arrhenius plots (**Figure S4**). For the SI catalysts the Ni_1 SI sample

provided the lowest value, namely 79 kJ mol^{-1}; the addition of Pd led to an almost monotonically increase of the E_a^{app}, achieving 122 kJ mol^{-1} for Pd_1 SI sample. For the DD samples, surprisingly, the lowest value was observed for Ni_5Pd_5 DD sample, namely 51 kJ mol^{-1}. Pd_1 DD showed the highest value 86 kJ mol^{-1} and the other catalysts presented activation energies in the range of 50-70 kJ mol^{-1}. These results show that the apparent activation energy is higher for pure Pd than with pure Ni. This can be explained by the electronic configuration of Pd, which has a lower d-band energy than Ni and, consequently, a lower reactivity.[21] Concerning the bimetallic NiPd DD samples, there is no clear correlation between metallic composition and E_a^{app}. But, increasing the Pd content up to 1Ni:1Pd led to a decrease in the energy barrier values; nevertheless, on Pd rich samples the values start to increase again, agreeing with the expected trend based on reactivity of both metals. Regarding CH_4 formation rate (r_{CH4}, Table 2) in general, higher Pd content led to a decrease of the r_{CH4} for the DD and SI samples, except for pure Pd. A good compromise between activity for CO_2 activation and selectivity towards RWGS was achieved with catalyst Ni_5Pd_5 DD, with E_a^{app} remarkably lower and a r_{CH4} lower than those of pure Ni catalyst.

2.3. Ni-Pd surface interaction and its influence on CO chemisorption

XPS results are summarized in **Table 3** and spectra presented on **Figure S4**. For the Ni_1 DD sample, there is a main Ni $2p_{3/2}$ peak centered at 853.4 eV, which is characteristic of NiO species. The small XPS peak at 852.5 eV is assigned to metallic Ni. For the Ni_5Pd_5 DD catalyst, a major peak is observed at ca. 855.0 eV, with a well-defined satellite at ca. 860 eV that can be assigned to $Ni(OH)_2$ species. The very low intense spectra of Ni_1Pd_9 DD sample show a main peak at 856.3 eV with a satellite at ca. 861.6 eV, again assigned to $Ni(OH)_2$ species, shifted to higher BEs, probably due to interaction with Pd. The Ni_1 and Ni_5Pd_5 SI samples both show a main peak at ca. 853 eV, characteristic of NiO species. Ni_1Pd_9 SI sample

also show a main peak shifted to higher BE values at 854.6 eV that can be assigned to NiO species, interacting with Pd.

At Pd 3d level, the DD samples showed contribution of two well-defined peaks typical of metallic Pd and PdO species: namely at ca. 335 and 336.6 eV for Pd_1 DD, 335 and 337 eV for Ni_1Pd_9 DD, and 334 and 335.8 eV for Ni_5Pd_5 DD, which might be shifted to lower BE values due to some interaction with Ni. For all SI samples, a higher concentration of metallic Pd was observed indicating that the HDA capping ligand limits surface oxidation of the NPs in some extent. For the Pd_1 SI and Ni_1Pd_9 SI samples, main peaks that are typical of metallic Pd and PdO species were found at ca. 335 and 337 eV, respectively. For the Ni_5Pd_5 SI two main peaks were observed at 335.6 and 337.8 eV, with a higher intensity for the last contribution, assigned to PdO.

The XPS data collected for the two sets of catalysts showed that in general the nanoparticles are in metallic state, with surface oxidation, in a core-shell like structure. The spectra of the parent metal catalysts (Ni_1 DD, Pd_1 DD, Ni_1 SI and Pd_1 SI) resemble to what can be expected for small nanoparticles of the respective elements. Importantly, for SI samples, the total metal content is lower than on DD ones, in good agreement with the metal content determined by ICP OES analysis. The bimetallic samples presented more complex spectra, which can be attributed to interaction between the Ni and Pd. At Ni 2p level, the presence of $Ni(OH)_2$ species detected for Ni_5Pd_5 and Ni_1Pd_9 DD samples indicates that segregation of Ni probably occurs, and that this Ni might be in close interaction with SiO_2 support that naturally has surface silicon hydroxyl species. For the bimetallic samples with higher Pd thus evidencing a contribution of the less oxophilic Pd metal that withdraws electron density from Ni. Likewise, at Pd 3d level, the spectrum of Ni_5Pd_5 DD sample is shifted to lower from charge transfer from Ni to Pd.[30]

If during the preparation of DD samples, there is formation of segregated Ni particles, however, the bimetallic NiPd structure might still be present. Due to the absence of capping

ligands detrimental interdiffusion process can occur and lead to element reconfiguration in the bimetallic nanoparticles[31]. Strong chemical bonds between Ni and hydrogen-containing adsorbates (such as surface hydroxyls) can also drive alloy segregation.[32] On the contrary, for the SI samples, the Pd showed lower PdO contribution, and the BE values agree better with that expected for Pd, except for Ni_5Pd_5 SI sample, that shows a higher contribution of PdO. The Ni 2p spectra showed mainly NiO species, with some charge transfer occurring on the Ni_1Pd_9 that can result from interaction with Pd, and lead to shifting of the spectrum to higher BE values.

The DRIFTS spectra recorded after CO chemisorption on the surface of reduced catalysts are shown in **Figure 4**. The high frequency (HF) bands in the region of 2080-2020 cm^{-1} are assigned to linear carbonyls bonded to metallic Ni, Pd sites. The low frequency (LF) bands at 2000-1850 cm^{-1} range are assigned to CO in multibond (bidentate, bridge and 3-fold configuration). The HF bands are associated with CO in weak bonding configuration to the metal surfaces ($*CO_w$), while, the LF bands correspond to CO strongly chemisorbed to the metal surface ($*CO_s$).[33] On pure Ni samples, bands at ca. 2020 cm^{-1} can be attributed to linear carbonyl species on planar crystal planes.[34] Linear carbonyls at ca. 2050 cm^{-1} visible on Ni samples (Figure 4), can be attributed to CO adsorbed on top of low-coordinated Ni,[34,35] a characteristic of highly dispersed Ni.[36] Comparing the two synthesis methodologies, on the Ni_1 DD, the 2050 cm^{-1} band is more prominent than that Ni_1 SI sample, which suggesting i) the presence of smaller NPs in the DD system or ii) the partial coverage of these low-coordinate sites by remaining HDA. The multibond species observed at ca. 1900 cm^{-1} can also give information about nanoparticle size and dispersion, with higher intensity bands being expected on larger NPs.[37] This can be observed on Ni_1 SI sample, where the band at 1910 cm^{-1} is significantly more intense than that in the linear region. On the Pd samples (Figure 4d), the multibond CO configurations are significantly larger than the linear ones. For DD samples, two bands are observed at ca. 1980 and 1955 cm^{-1}, as well as low intensity HF

($*CO_w$) bands at ca. 2055 and 2075 cm^{-1}. On the other hand, for the SI, a very intense band at ca. 1945 is visible ($*CO_s$); also, the HF bands are very low intense.

CO chemisorption probed by FTIR is a powerful tool in order to investigate metal nanoparticles characteristics, such as particle size, electron density on surface, exposed facets, support interactions, nature and population of different active sites.[38] Nevertheless, the independent investigation of these features is difficult. The higher $*CO_s$ intensities compared to those of $*CO_w$ for pure Pd catalysts, is reported in the literature to occur at lower CO coverages (symbolized as θ).[39] The linear modes appear as the coverage increases (θ=0.75). In terms of nanoparticle size, different interpretations are reported in the literature. Szanyi and Goodman[40] describe that on small nanoparticles of ca. 10-50 atoms, linear Pd carbonyls dominate in opposition of bridging CO. However, with Pd nanoparticles such as those presented here, and the DRIFTS configuration, with high CO partial pressures, the very low intensity of $*CO_w$ bands observed (Figure 5d, right) can be explained by the presence of remaining hexadecylamine capping ligand more strongly bonded to low coordinated Pd sites on the Pd SI sample. This is supported by the fact that the presence of HDA was observed by N 1s XPS spectra in significant surface concentration, even higher than Ni+Pd ones (Table 3). In the Ni case, the higher predominance of linear CO modes (Figure 4a), is indicative of a more heterogeneous surface, with terrace planar sites and edge sites in similar proportion; it also indicates a higher reactivity of the Ni sites, due to higher density of Ni in low-coordination configuration.

The higher intensity of linear carbonyls observed on Ni_5Pd_5 DD compared to other samples can be explained by 1) changing the NiPd alloy metal bond length in terms that it can hinder the CO in multibond configuration and 2) increase of low coordinated Ni,Pd sites, that are more prone to adsorb linear carbonyls, in the form of $Ni,Pd(CO)_4$; as these sites are more reactive, the CO bonding strength is lower and can be desorbed easily. For more clarity, the E_a^{app} and the ratio of CO weakly to CO strongly ($*CO_w/*CO_s$) bonded to surface are plotted

as function of Pd molar fraction (**Figure 5**). The higher presence of low-coordinated sites is the consequence of smaller nanoparticle sizes, like that encountered in Ni_5Pd_5 DD sample (Table 1, Figure 5). Nevertheless, a compensation of the amount of such low coordinated sites (particle size) and the nature of the metal dictates the reactivity. As showed by Dietz *et al*., the binding energy of CO to Pd surfaces is slightly lower than to Ni surfaces,[22] whereas the O binding energy to Ni (-5.69 eV) is significantly lower than on Pd (-4.75 eV). It is worth noting that binding energy is defined as the total energy of slab with chemisorbed molecule minus the sum of the total energies of clean slab and free molecule, thus a more negative value indicates a more exothermic chemisorption.[22,23] Therefore, Ni sites are more reactive towards O and less stable CO are formed on Ni compared to Pd; chemisorbed CO can be more stable on less reactive Pd surface. These literature data are in good accordance with our experimental observations, where the Pd-rich samples are in general less active than Ni-rich ones, with conversion degrees significantly lower at a given temperature. On the SI samples, the weak HDA ligand can bond preferentially to the most reactive low coordinated metallic sites, which are the ones expected to adsorb CO linearly, and deliver gas phase CO. This is in good agreement with both the E_a^{app} values and the low $*CO_w/*CO_s$ ratio values encountered for this set of samples. In terms of selectivity, in general the Pd-rich samples are less prone to CO_2, CO hydrogenation to CH_4. The CO-DRIFTS and reactivity results show that if the Pd NPs were active in the same temperature range than Ni, CH_4 formation was supposed to be significantly higher than on Ni NPs, taking into account the lower binding energy of CO on Pd surfaces compared to Ni.[22,23] However, at the temperature ranges where Pd is active, in this case, CH_4 formation from Sabatier (Equation 1) reaction is not favored.

$$CO_2 + 4H_2 \rightarrow CH_4 + 2H_2O \qquad \Delta H^0_{298K} = -165.08\ kJ\ mol^{-1} \tag{1}$$

These findings are pointing out to the different nanoparticle self-assembling process. Without SiO_2 in the medium but with capping ligands, the decomposition of organometallic

precursors follows the adequate kinetic control to produce Ni-Pd nuclei. Without the capping ligands, the assembling of the Ni and Pd nuclei was more difficult, and even more due to the presence of SiO_2, which address the fast metal deposition on its surface, two parameters that do not allow the formation of bimetallic alloy. The higher $Ni(COD)_2$ reactivity drives the formation of small nanoclusters, interacting strongly with the surface, helped by the -OH terminations on the surface. $Pd_2(dba)_3$ precursor, on the contrary, can produce nanoparticles easily in such conditions. These different arrangements are directly related to the catalytic activity in a model reaction such as RWGS.

3. Conclusion

Two synthesis methodologies were explored in order to produce well-defined bimetallic NiPd nanoparticles starting from organometallic complexes at the metal source, focusing on the catalytic activity for CO_2 conversion. Nanoparticles with average nanoparticle sizes in the range of 3 to 6 nm were pre-stabilized with HDA and then deposited onto SiO_2 by simple impregnation method which led to metal loadings ranging from 0.6 to 1.0 wt% (SI samples). XPS and TEM analyses showed the formation of nanoalloys whatever the Ni/Pd ratio. When the decomposition of the organometallic precursors was performed directly onto SiO_2 and in the absence of capping ligands, the decomposition and nucleation process were boosted, which did not allow the formation of nanoalloys. These DD samples showed a total metal content in the range 2 to 3 wt% that contained nanoparticles of mean sizes ranging from 3 to 4 nm. The XPS and TEM investigation showed that segregated Pd nanoparticles and very small Ni nanoclusters were produced in that case.

The obtained two sets of catalysts were then applied in the CO_2 transformation into CO focusing on RWGS model reaction. SI samples showed a typical behavior of the conversion rate shifting to higher temperatures with increasing of Pd content. Selectivity to CO improved following the same trend, which can be due to the CO_2 conversion in temperature regimes

were CH_4 is unfavorable. On the contrary, the DD samples appeared active for CO_2 activation at lower temperatures compared to their SI counterparts, which can be explained by the absence of capping ligands and the general lower nanoparticle sizes, especially the Ni-containing catalysts, for which the results obtained led us to conclude that more active isolated Ni clusters are present. With Ni:Pd ratio of 1:1, surprisingly, the conversion degree and selectivity to CH_4 and CO is similar to pure Ni, but with a lower energy barrier for CO_2 conversion; the bimetallic Pd-rich sample presented a behavior more close to pure Pd. This finding was consistent with characterization results that showed the very small Ni nanoclusters segregated from Pd nanoparticles, which in turn are more active than the pure Ni samples themselves.

The FTIR analysis of chemisorbed CO showed that CO was preferentially chemisorbed strongly in bidentate and 3-fold configurations on Pd-rich samples while on Ni-rich ones the linear CO configuration arose. This helped to understand why the Ni-rich samples were more active: the CO weakly bonded to Ni surface is more available to desorb as gas phase CO and to be hydrogenated to CH_4 under reaction conditions. These findings helped to understand how the synthesis protocol changed the structure of bimetallic nanoparticles and the consequent behavior under reaction conditions.

4. Experimental Section

Catalyst Preparation

Magnetic core-shell Fe_3O_4@SiO_2 support material was used for the preparation of the catalysts in order to facilitate their separation being air sensitive synthesis systems. The magnetic support was prepared *via* a reverse microemulsion route, and further functionalized by a surface reaction with 3-aminopropiltrietoxysilane (APTES), in order to facilitate the

impregnation of the nanoparticles, as described in a previous work.[41] No magnetite particles were found outside the SiO_2 shell.

The preparation of the catalysts was performed following two different methods: 1) immobilization of preformed colloidal nanoparticles on the functionalized silica support by simple impregnation, samples identified as SI (sol-immobilization method) and 2) direct co-decomposition of the organometallic precursors over the support without capping ligand, samples identified as DD (direct decomposition). The metal precursors were used as received and handled in a glove box under Ar atmosphere; the solvents were dried and degassed using standard air sensitive procedures.

The set of SI samples were prepared by a procedure previously described:[26] briefly, Ni and Pd precursors, $Ni(cod)_2$ and $Pd_2(dba)_3$, respectively, in desired amounts to give nominal proportions of Ni, 1Ni:1Pd, 1Ni:9Pd and Pd (total 0.9 mmol) were introduced in a Fisher-Porter reactor under inert atmosphere and placed in a cryogenic bath. Then, a toluene solution (30 mL) of hexadecylamine (0.3 mol L^{-1}) was added. The reactor was then evacuated (0.2 torr) and pressurized under H_2 (3 bar), and the cold bath removed before heating to 110^{o}C (silicon oil bath). Vigorous stirring was maintained up to 20 h, leading to a black colloidal dispersion containing metal nanoparticles. Afterwards, the NP immobilization was performed as follows: functionalized SiO_2 (1 g) support (outgassed for 1 h under vacuum) was introduced into a Schlenk flask followed by the colloidal dispersion (6 mL); the mixture was stirred at R.T. under Ar atmosphere for 2 h. The obtained grey solid was magnetically recovered from the dispersion by simple application of a magnet, and the supernatant was removed with a syringe. The final solid was then dried under vacuum for 1 h (0.2 torr) and stored under inert conditions until use in characterization and catalytic testes.

The set of DD samples was prepared as follows: the functionalized SiO_2 (1 g) support was introduced into a Fisher-Porter reactor, followed by air evacuation (0.2 torr) and filling with Ar. Toluene solution (25 mL) of Ni and Pd precursors (0.45 mmol mL^{-1}; at desired Ni/Pd

ratios) was prepared in a Schlenk flask, under Ar atmosphere. This solution was then transferred to the SiO_2 containing reactor, followed by outgassing under vacuum and pressurization with H_2 (3 bar). The mixture was then stirred for 1 h at R.T. Afterwards, the solid was washed with dried toluene 5 times, under Ar atmosphere. The final solid was magnetically recovered by simple application of a magnet and dried under vacuum (0.2 torr) for 1 h and stored under air conditions.

The catalysts were labeled as Ni_xPd_y *DD* for the direct decomposition method and Ni_xPd_y *SI* for the sol-immobilization method, with the *x* and *y* numbers referring to the nominal Ni:Pd molar ratio (1:0, 1:1, 1:9, 0:1).

Characterization

Ni and Pd contents in the catalysts were determined by ICP-OES. The samples (10 mg) were digested in aqua regia solution (10 mL) at 100ºC for 3 h and analyzed in a Spectro Ciros equipment.

The surface composition of the catalysts was studied by X-ray photoelectron spectroscopy (XPS), using a conventional XPS spectrometer (ScientaOmicron ESCA+) with a high-performance hemispheric analyzer (EAC2000) with monochromatic Al Kα ($h\nu$ = 1486.6 eV) radiation as the excitation source. The as prepared catalysts were deposited on a carbon tape and loaded to the XPS equipment. The base vacuum was 10^{-9} torr. The XPS high-resolution spectra were recorded at a constant pass energy of 20 eV with an energy step of 0.05 eV. The fitting of the XPS components was performed using a Gaussian/Lorentzian function (30/70), and binding energy was referred to the C 1s level of adventitious carbon (284.6 eV).

Transmission electron microscopy was used to evaluate the particle size distribution and morphology. The images were obtained at a Jeol JEM 2100F microscope, with a field emission gun accelerated at 200 kV. The as prepared catalysts were dispersed in isopropyl

alcohol with sonication, and the dispersion was dripped on a lacey carbon coated cupper grid. The images were acquired in conventional TEM and scanning TEM mode. The particle size distribution was estimated by fitting of histograms with a log-normal function. High-resolution STEM images and EDS mapping were acquired on aberration corrected FEI Titan Themis^3 equipment, with acceleration voltage of 300 kV; compositional EDS mapping was obtained with an Espirit system.

DRIFTS of adsorbed CO was performed in order to probe the differences in electronic densities and catalytic sites of the catalysts. The experiments were performed in a commercial Harrick high-temperature cell and spectra were acquired on a Thermo iS50R spectrometer, equipped with an MCT detector (resolution 4 cm^{-1} and 64 scans). The as prepared samples were loaded into the cell with a subsequent thermal treatment under 5% H_2/He mixture, at 400°C for 1 h. Then, the samples were cooled down to R.T. under He flow, when the background spectrum was acquired. The CO adsorption was performed by flowing 10 mL/min of a 5% CO/He diluted in 10 mL/min of pure He; the CO flow passed through the sample for 5 min. After, the flow was switched to He to desorb the gas phase CO, with spectra acquisition.

Catalytic evaluation

The RWGS catalytic tests were performed using a fixed bed quartz reactor, at atmospheric pressure, from 200 to 700°C, in steps of 50°C, in a CatLab PCS unit (Hiden Analytical). Due to different metal loading achieved during synthesis, the catalyst mass was adjusted in order to have 0.5 mg of metal in total (Ni+Pd). Thus, total mass in the range of 10-20 mg was used for the series of catalysts prepared by direct decomposition (DD); and of 15-40 mg for the catalysts prepared by sol-immobilization (SI). All the catalysts were previously thermally treated at 400°C, for 30 min, under flow of a 5% H_2/Ar mixture, in order to recover a fully metallic surface. Afterwards, the catalysts were cooled down to 100°C, and the reaction

proceeded up to 700°C, with reaction data acquisition on each 50°C step, for 30 minutes, to reach steady state conditions. The product formation was evaluated using a calibrated mass spectrometer (Hiden Analytical). The gas composition applied for the catalysis tests was 2% CO_2 / 2% H_2 / Ar balance and a total gas flow of 100 mL min^{-1}. The reaction rate was evaluated following the Equation 2, where r_{CO2} is the experimental reaction rate (in mol s^{-1} g_{metal}^{-1}), X is the conversion degree, F_{CO2} is the CO_2 inlet flow (mol s^{-1}) and W_{metal} the metal mass (in g). Arrhenius plots were obtained from the reaction rates calculated at maximum conversions of 25%, and the apparent activation energy values (E_a^{app}, in kJ mol^{-1}) were obtained from fitting of the experimental data.

Supporting Information
Supporting Information is available from the Wiley Online Library or from the author.

Acknowledgements
We gratefully acknowledge support of the RCGI – Research Centre for Gas Innovation, hosted by the University of São Paulo (USP) and sponsored by FAPESP – São Paulo Research Foundation (2014/50279-4) and Shell Brasil. Acknowledgements are given to Brazilian Nanotechnology Laboratory, LNNano, for use of TEM facilities (proposal #TEM-24456). All authors contributed equally.

Received: ((will be filled in by the editorial staff))
Revised: ((will be filled in by the editorial staff))
Published online: ((will be filled in by the editorial staff))

References

[1] M. Roiaz, E. Monachino, C. Dri, M. Greiner, A. Knop-Gericke, R. Schlögl, G. Comelli, E. Vesselli, *J. Am. Chem. Soc.* **2016**, *138*, 4146.

[2] M. A. Atanga, F. Rezaei, A. Jawad, M. Fitch, A. A. Rownaghi, *Appl. Catal. B Environ.* **2018**, *220*, 429.

[3] E. C. Lovell, A. Fuller, J. Scott, R. Amal, *Appl. Catal. B Environ.* **2016**, *199*, 155.

[4] S. C. M. Mizuno, A. H. Braga, C. E. Hori, J. B. O. Santos, J. M. C. Bueno, *Catal. Today* **2017**, *296*, 144.

[5] R. V. Gonçalves, L. L. R. Vono, R. Wojcieszak, C. S. B. Dias, H. Wender, E. Teixeira-Neto, L. M. Rossi, *Appl. Catal. B Environ.* **2017**, *209*, 240.

[6] J. C. Matsubu, V. N. Yang, P. Christopher, *J. Am. Chem. Soc.* **2015**, *137*, 3076.

[7] J. Sehested, S. Dahl, J. Jacobsen, J. R. Rostrup-Nielsen, *J. Phys. Chem. B* **2005**, *109*, 2432.

[8] H. Falsig, B. Hvolbæk, I. S. Kristensen, T. Jiang, T. Bligaard, C. H. Christensen, J. K. Nørskov, *Angew. Chemie - Int. Ed.* **2008**, *47*, 4835.

[9] P. Munnik, M. E. Z. Velthoen, P. E. de Jongh, K. P. de Jong, C. J. Gommes, *Angew. Chemie Int. Ed.* **2014**, *126*, 9647.

[10] X. Wang, H. Shi, J. H. Kwak, J. Szanyi, *ACS Catal.* **2015**, *5*, 6337.

[11] C. Vogt, E. Groeneveld, G. Kamsma, M. Nachtegaal, L. Lu, C. J. Kiely, P. H. Berben, F. Meirer, B. M. Weckhuysen, *Nat. Catal.* **2018**, *1*, 127.

[12] B. Miao, S. S. K. Ma, X. Wang, H. Su, S. H. Chan, *Catal. Sci. Technol.* **2016**, *6*, 4048.

[13] H. C. Wu, Y. C. Chang, J. H. Wu, J. H. Lin, I. K. Lin, C. S. Chen, *Catal. Sci. Technol.* **2015**, *5*, 4154.

[14] A. H. Braga, E. R. Sodré, J. B. O. Santos, C. M. de Paula Marques, J. M. C. Bueno, *Appl. Catal. B Environ.* **2016**, *195*, 16.

[15] K. A. Resende, A. H. Braga, F. B. Noronha, C. E. Hori, *Appl. Catal. B Environ.* **2019**, *245*, 100.

[16] M. Li, H. Amari, A. C. van Veen, *Appl. Catal. B Environ.* **2018**, *239*, 27.

[17] S. Yao, L. Lin, W. Liao, N. Rui, N. Li, Z. Liu, J. Cen, F. Zhang, X. Li, L. Song, L. Betancourt De Leon, D. Su, S. D. Senanayake, P. Liu, D. Ma, J. G. Chen, J. A. Rodriguez, *ACS Catal.* **2019**, 9087.

[18] Y. Dai, Y. Wang, B. Liu, Y. Yang, *Small* **2015**, *11*, 268.

[19] A. B. Hungría, N. D. Browning, R. P. Erni, M. Fernández-garcía, J. C. Conesa, J. A. Pérez-Omil, A. Martínez-Arias, *J. Catal.* **2005**, *235*, 251.

[20] A. B. Hungría, M. Fernández-garcía, J. A. Anderson, A. Martínez-Arias, *J. Catal.* **2005**, *235*, 262.

[21] J. H. Larsen, I. Chorkendorrf, *Surf. Sci. Rep.* **1999**, *35*, 163.

[22] L. Dietz, S. Piccinin, M. Maestri, *J. Phys. Chem. C* **2015**, *119*, 4959.

[23] S. G. Wang, X. Y. Liao, D. B. Cao, C. F. Huo, Y. W. Li, J. Wang, H. Jiao, *J. Phys. Chem. C* **2007**, *111*, 16934.

[24] G. Guisbiers, R. Mendoza-Pérez, L. Bazán-Díaz, R. Mendoza-Cruz, J. Velázquez-Salazar, M. José-Yacamán, *J. Phys. Chem. C* **2017**, *121*, 6930.

[25] N. J. S. Costa, R. F. Jardim, S. H. Masunaga, D. Zanchet, R. Landers, L. M. Rossi, *ACS Catal.* **2012**, *2*, 925.

[26] N. J. S. Costa, M. Guerrero, V. Collière, É. Teixeira-Neto, R. Landers, K. Philippot, L. M. Rossi, *ACS Catal.* **2014**, *4*, 1735.

[27] C. Amiens, B. Chaudret, D. Ciuculescu-Pradines, V. Collière, K. Fajerwerg, P. Fau, M. Kahn, A. Maisonnat, K. Soulantica, K. Philippot, *New J. Chem.* **2013**, *37*, 3374.

[28] D. Baudouin, C. Szeto, P. Laurent, A. De Mallmann, B. Fenet, L. Veyre, U. Rodemerck, C. Cope, C. Thieuleux, *J. Am. Chem. Soc.* **2012**, *134*, 20624.

[29] N. Shang, X. Zhou, C. Feng, S. Gao, Q. Wu, C. Wang, *Int. J. Hydrogen Energy* **2017**, *42*, 5733.

[30] C. Zhu, D. Wen, M. Oschatz, M. Holzschuh, W. Liu, A. K. Herrmann, F. Simon, S. Kaskel, A. Eychmüller, *Small* **2015**, *11*, 1430.

[31] K. D. Gilroy, A. Ruditskiy, H. C. Peng, D. Qin, Y. Xia, *Chem. Rev.* **2016**, *116*, 10414.

[32] L. Pielsticker, I. Zegkinoglou, N. J. Divins, H. Mistry, Y. T. Chen, A. Kostka, J. A. Boscoboinik, B. R. Cuenya, *J. Phys. Chem. B* **2018**, *122*, 919.

[33] X. Wang, H. Shi, J. Szanyi, *Nat. Commun.* **2017**, *8*, 1.

[34] G. Garbarino, S. Campodonico, A. R. Perez, M. M. Carnasciali, P. Riani, E. Finocchio, G. Busca, *Appl. Catal. A Gen.* **2013**, *452*, 163.

[35] K. Hadjiivanov, M. Mihaylov, D. Klissurski, P. Stefanov, N. Abadjieva, E. Vassileva, L. Mintchev, *J. Catal.* **1999**, *185*, 314.

[36] G. Martra, H. M. Swaan, C. Mirodatos, M. Kermarec, C. Louis, *Stud. Surf. Sci. Catal.* **1997**, *111*, 617.

[37] C. D. Zeinalipour-Yazdi, D. J. Willock, L. Thomas, K. Wilson, A. F. Lee, *Surf. Sci.* **2016**, *646*, 210.

[38] C. D. Zeinalipour-Yazdi, D. J. Willock, L. Thomas, K. Wilson, A. F. Lee, *Surf. Sci.* **2016**, *646*, 210.

[39] I. V. Yudanov, R. Sahnoun, K. M. Neyman, N. Rösch, J. Hoffmann, S. Schauermann, V. Johánek, H. Unterhalt, G. Rupprechter, J. Libuda, H. J. Freund, *J. Phys. Chem. B* **2003**, *107*, 255.

[40] J. Szanyi, D. W. Goodman, *J Phys Chem* **1994**, *98*, 2972.

[41] M. J. Jacinto, P. K. Kiyohara, S. H. Masunaga, R. F. Jardim, L. M. Rossi, *Appl. Catal. A Gen.* **2008**, *338*, 52.

Table 1. Metal content, bulk Pd concentration, surface Pd concentration and average particle size for the as prepared NiPd catalysts.

Catalysts	Metal content [%][a)]		Bulk Pd/(Pd+Ni) ratio [%][b)]	Surface Pd/(Pd+Ni) ratio [%][c)]	Particle size [nm][d)]
	Ni	Pd			
Ni_1 DD	2.64		-	-	4.4±1.5
Ni_5Pd_5 DD	1.33	2.01	60.2	59.9	3.7±0.7
Ni_1Pd_9 DD	0.30	3.69	92.5	95.0	3.2±0.1
Pd_1 DD		3.29	100	100	3.5±0.8
Ni_1 SI	0.64		-	-	6.3±1.3
Ni_5Pd_5 SI	0.43	0.63	59.4	61.3	4.2±1.0
Ni_1Pd_9 SI	0.05	0.68	93.2	96.5	5.3±1.0
Pd_1 SI		0.80	100	100	5.8±1.4

[a)] Metal composition determined by ICP OES; [b)] Bulk Pd/(Ni+Pd) ratio calculated from ICP OES results; [c)] Surface Pd/(Ni+Pd) ratio calculated from surface composition determined by XPS; [d)] Average particle size measured by TEM.

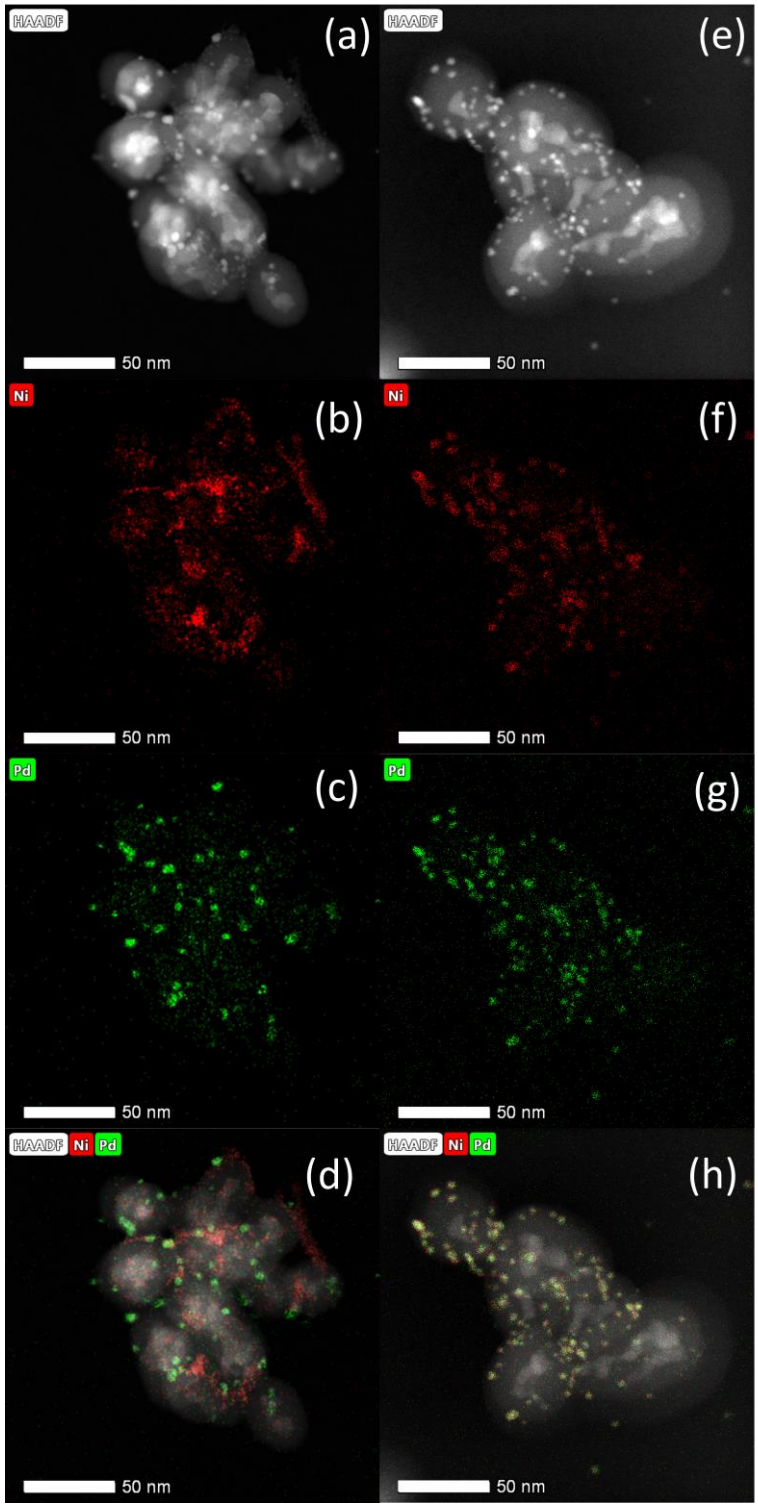

Figure 1. STEM-HAADF image of the Ni_5Pd_5 DD (a) and EDS elemental analysis of Ni (b), Pd (c) with color mix image (d); and STEM-HAADF image of Ni_5Pd_5 SI (e) with the corresponding Ni (f), Pd (g) and color mix image (h) elemental mappings.

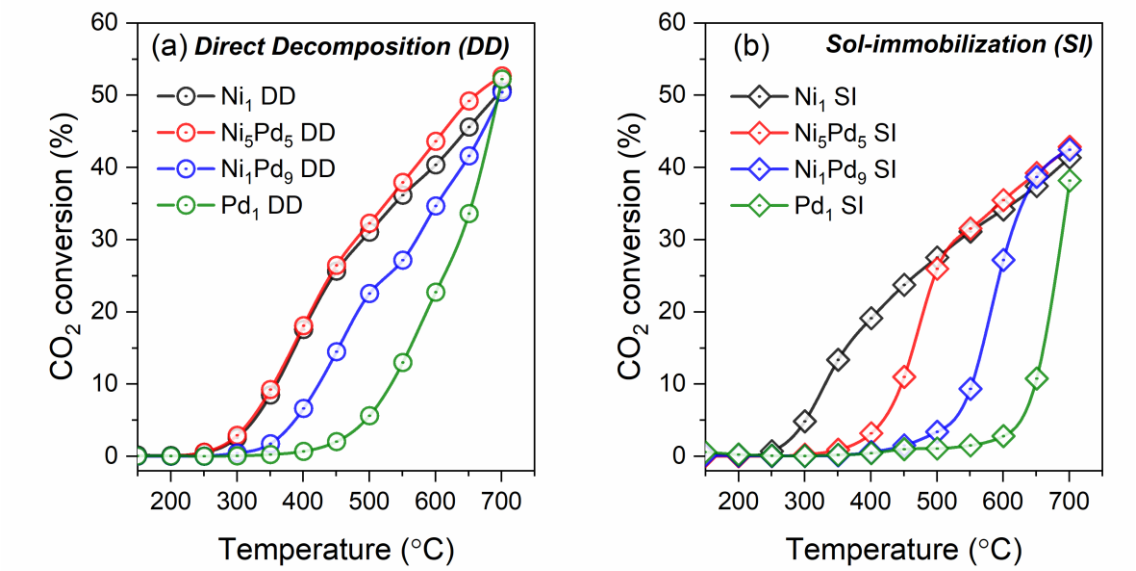

Figure 2. CO_2 conversion as function of temperature for the series of Ni-Pd catalysts prepared from Direct Deposition, *DD*, (a) and Sol-Immobilization, *SI*, (b) methodologies. Samples were pre-treated under H_2 at 400ºC for 30 min; W_{metal}=0.5 mg of total metal (Ni+Pd); 1 CO_2:4 H_2:45 Ar.

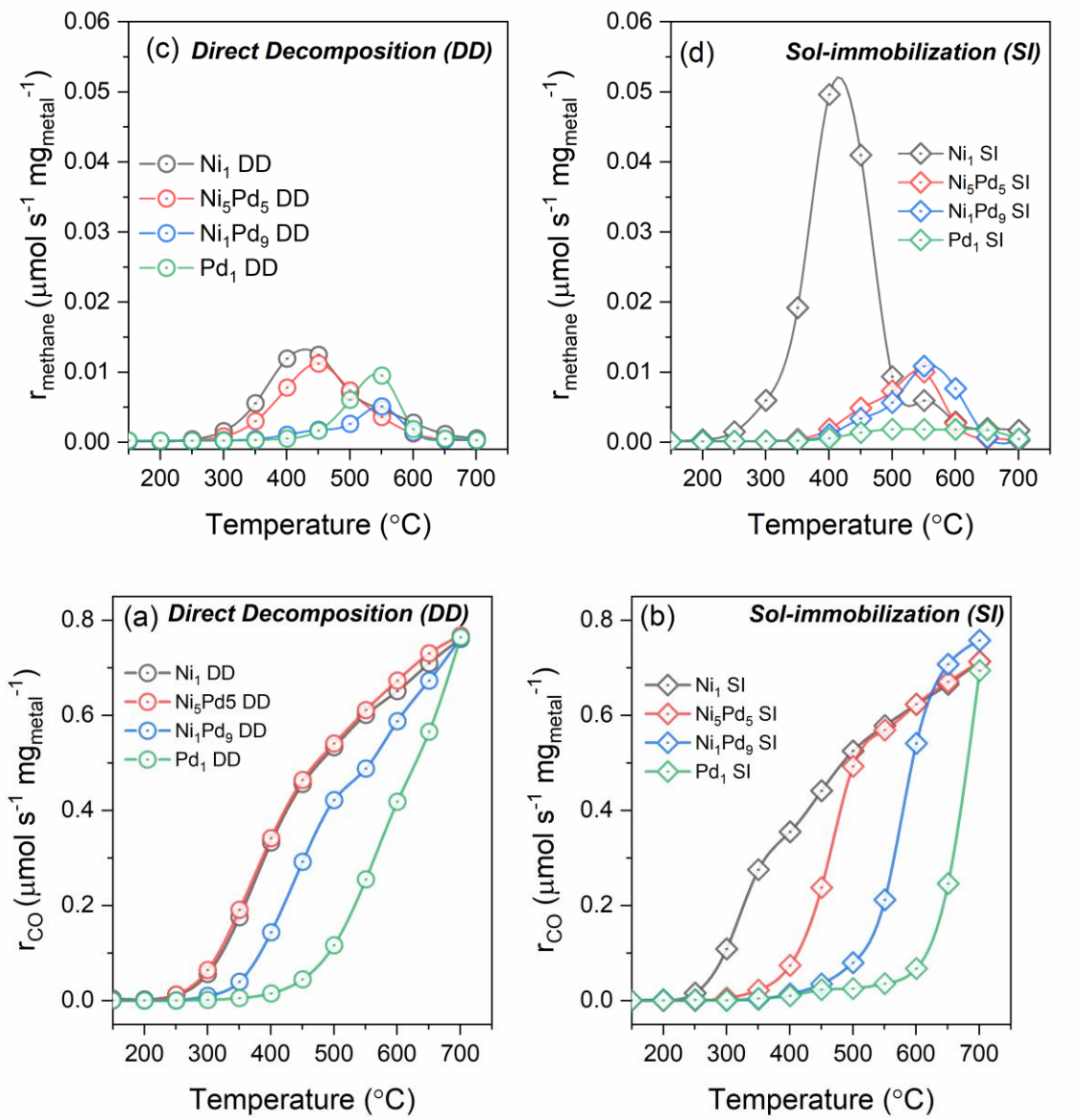

Figure 3: Rates of CO (a,b) and CH_4 (c,d) formation from RWGS as function of temperature for the series of NiPd catalysts prepared from Direct Deposition, *DD*, (a,c) and Sol Immobilization, *SI*, (b,d) methodologies. Samples were pre-treated under H_2 at 400ºC for 30 min; W_{metal}=0.5 mg of total metal (Ni+Pd); 1 CO_2:4 H_2:45 Ar.

Table 2: Overall CH_4 formation rate and apparent activation energy obtained for SI and DD reduced catalysts at 400°C, 30 min under H_2.

Catalyst	Total r_{CH4} [µmol $s^{-1}g_{metal}^{-1}$]	E_a^{app} [kJ mol^{-1}]
Ni_1 DD	2.0	73.4
Ni_5Pd_5 DD	1.5	51.1
Ni_1Pd_9 DD	0.5	69.1
Pd_1 DD	0.8	85.5
Ni_1 SI	5.9	78.9
Ni_5Pd_5 SI	1.2	88.2
Ni_1Pd_9 SI	1.2	91.2
Pd_1 SI	2.0	121.8

Table 3: Binding energies of Ni $2p_{3/2}$ main peak, Pd 3d regions and surface metal composition (at. %) obtained from XPS of the as prepared catalysts.

Catalyst	Binding energies [eV]			Surface composition [at%]	
	Ni $2p_{3/2}$	Pd $3d_{5/2}$	Pd $3d_{3/2}$	Ni	Pd
Ni_1 DD	855.8			0.4	
Ni_5Pd_5 DD	855.0	334.4	335.8	0.7	1.1
Ni_1Pd_9 DD	856.3	335.6	337.3	0.1	2.0
Pd_1 DD		335.1	336.6		1.8
Ni_1 SI	853.3			0.3	
Ni_5Pd_5 SI	853.1	335.6	337.5	0.3	0.5
Ni_1Pd_9 SI	854.6	335.2	337.0	0.04	1.1
Pd_1 SI		335.5	337.5		1.0

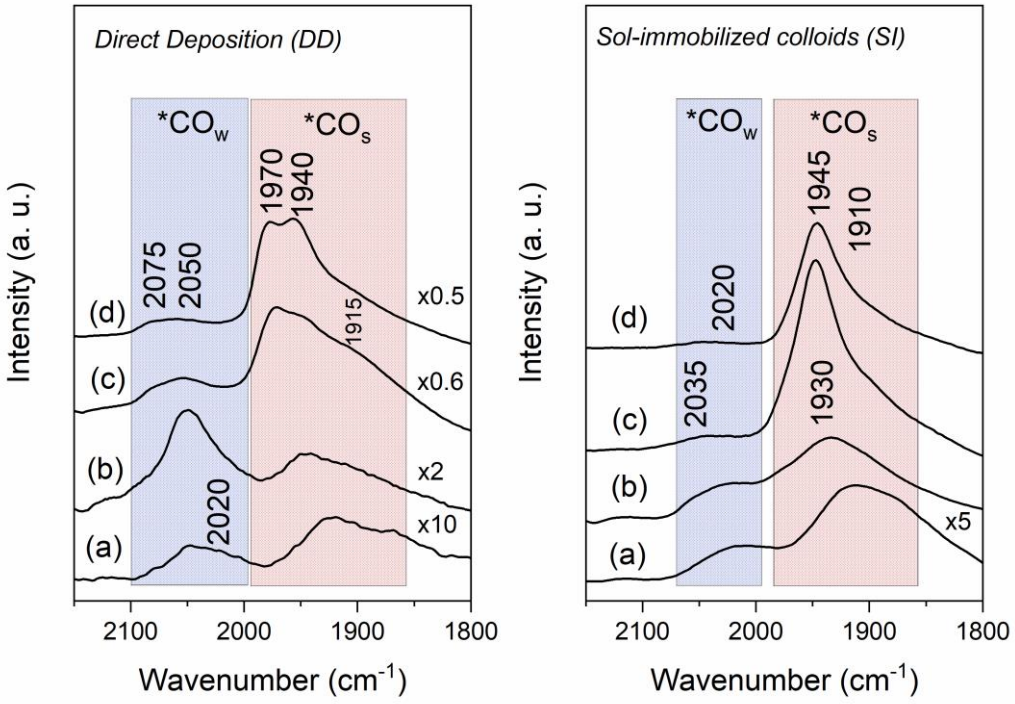

Figure 4: DRIFTS spectra of adsorbed CO at room temperature onto the reduced catalysts at 400ºC, for 1h. (left) Ni_xPd_y DD samples; (right) Ni_xPd_y SI samples. (a) Ni_1, (b) Ni_5Pd_5, (c) Ni_1Pd_9, (d) Pd_1.

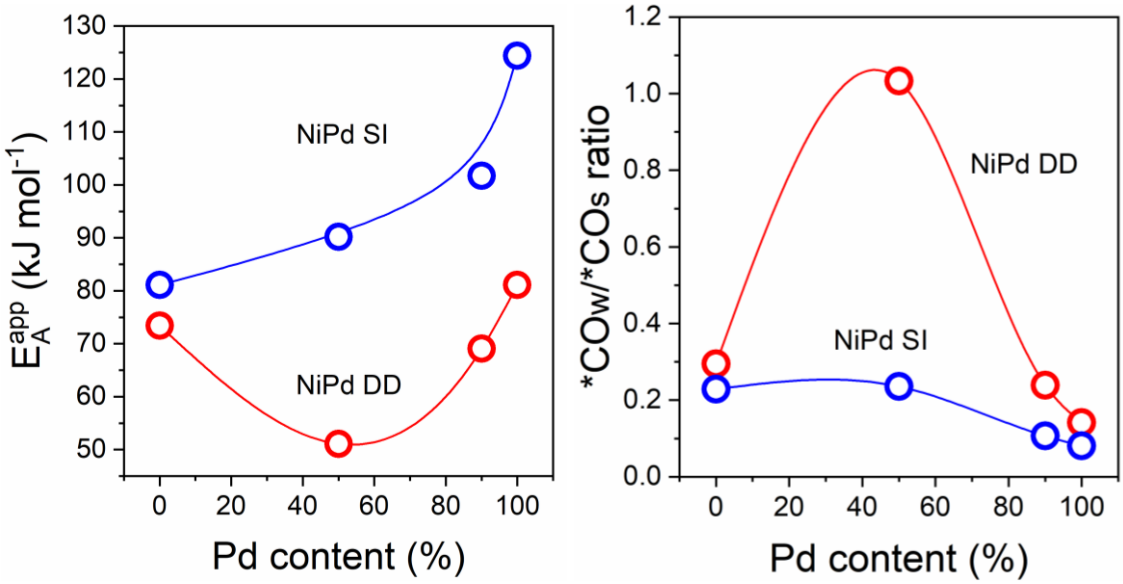

Figure 5: Correlation between the Apparent Activation Energies (E_a^{app}) and weakly to strongly adsorbed CO ratio ($*CO_w/*CO_s$) with Pd content.

Rational design of bimetallic Ni-Pd/SiO_2 catalysts for CO_2 transformation. Synthesis methodologies directly influences the catalyst activity, by forming alloyed NPs or segregated phases. Direct decomposing organometallic precursors on SiO_2 without stabilizers produces small Ni clusters and Pd nanoparticles. Surprisingly, the small Ni cluster are responsible for the lowest energy barrier for CO_2 activation.

Keyword

Adriano H. Braga, Natália J. S. Costa, Karine Phillipot, Renato V. Gonçalves, János Szanyi, Liane M. Rossi*

Structure and activity of bimetallic NiPd nanoparticles: influence of preparation method on CO_2 conversion through RWGS

ToC figure ((Please choose one size: 55 mm broad × 50 mm high or 110 mm broad × 20 mm high. Please do not use any other dimensions))

Supporting Information

Structure and activity of bimetallic NiPd nanoparticles: influence of preparation method on CO_2 conversion through RWGS

*Adriano H. Braga, Natália J. S. Costa, Karine Phillipot, Renato V. Gonçalves, János Szanyi, Liane M. Rossi**

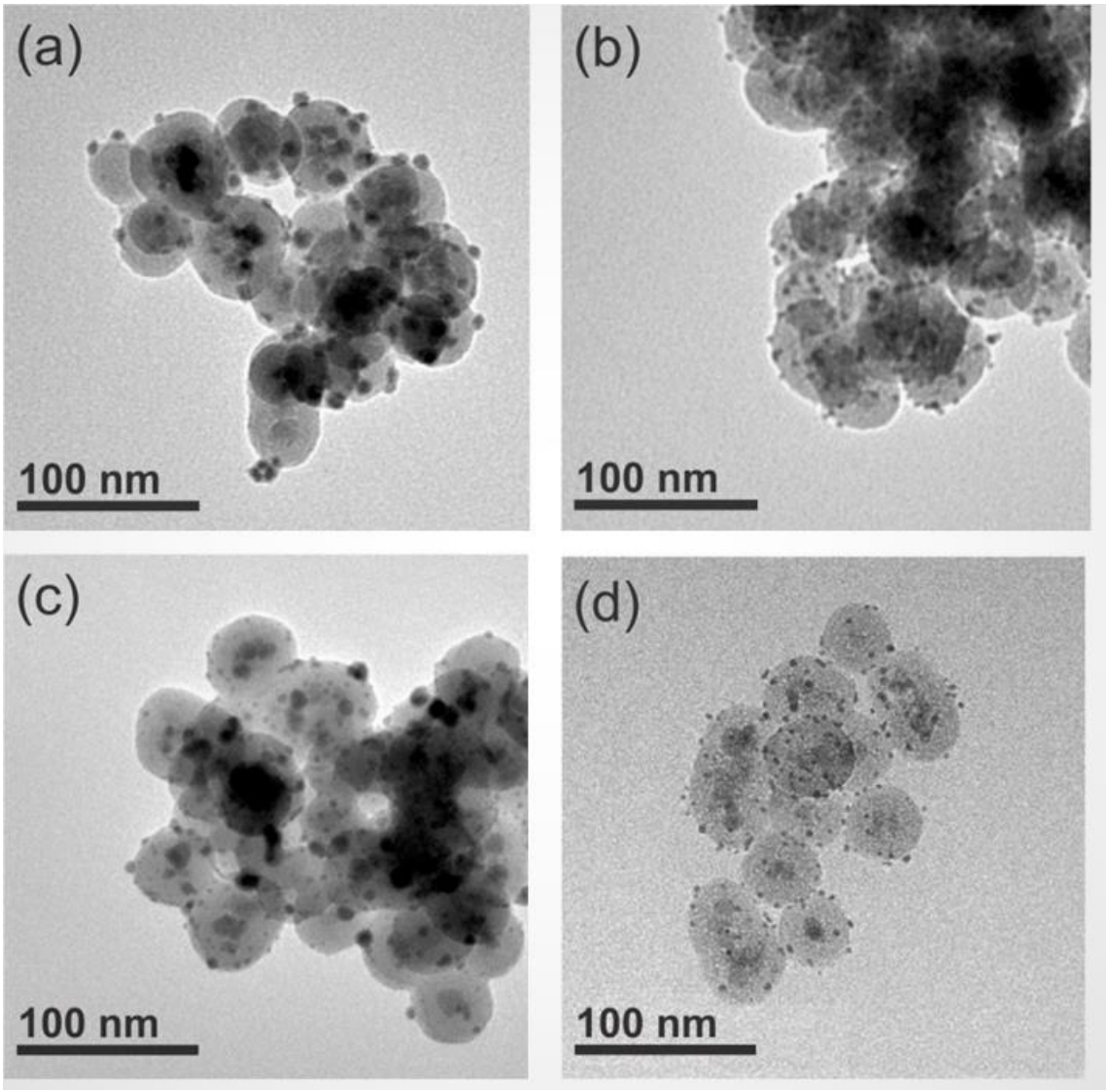

Figure S1: TEM images of the as prepared DD samples: (a) Ni_1 DD, (b) Ni_5Pd_5 DD, (c) Ni_1Pd_9 DD and (d) Pd_1 DD.

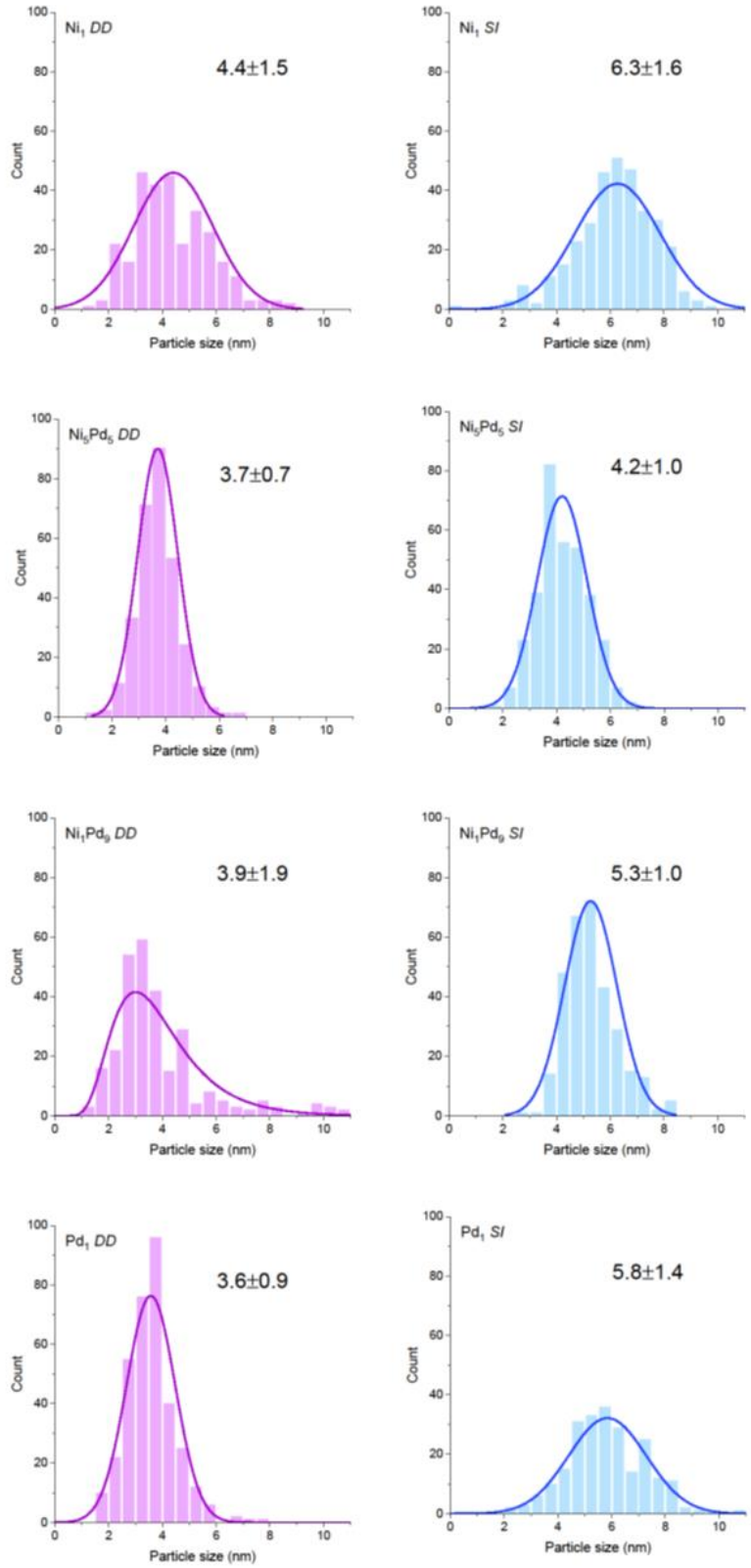

Figure S2: Particle size distribution of the as prepared samples.

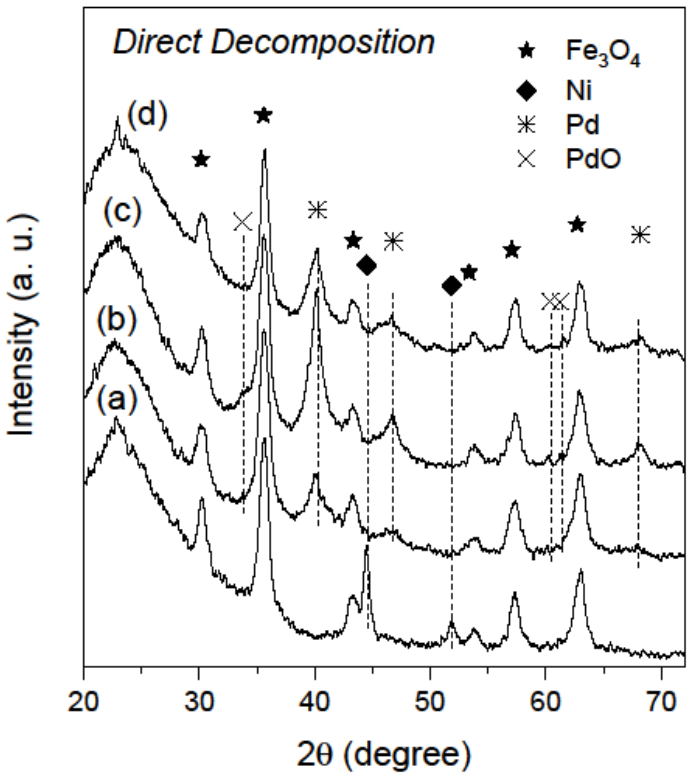

Figure S3: X-ray diffraction patterns of the as prepared Ni_xPd_y DD samples (a) Ni_1 DD, (b) Ni_5Pd_5 DD, (c) Ni_1Pd_9 DD and (d) Pd_1 DD.

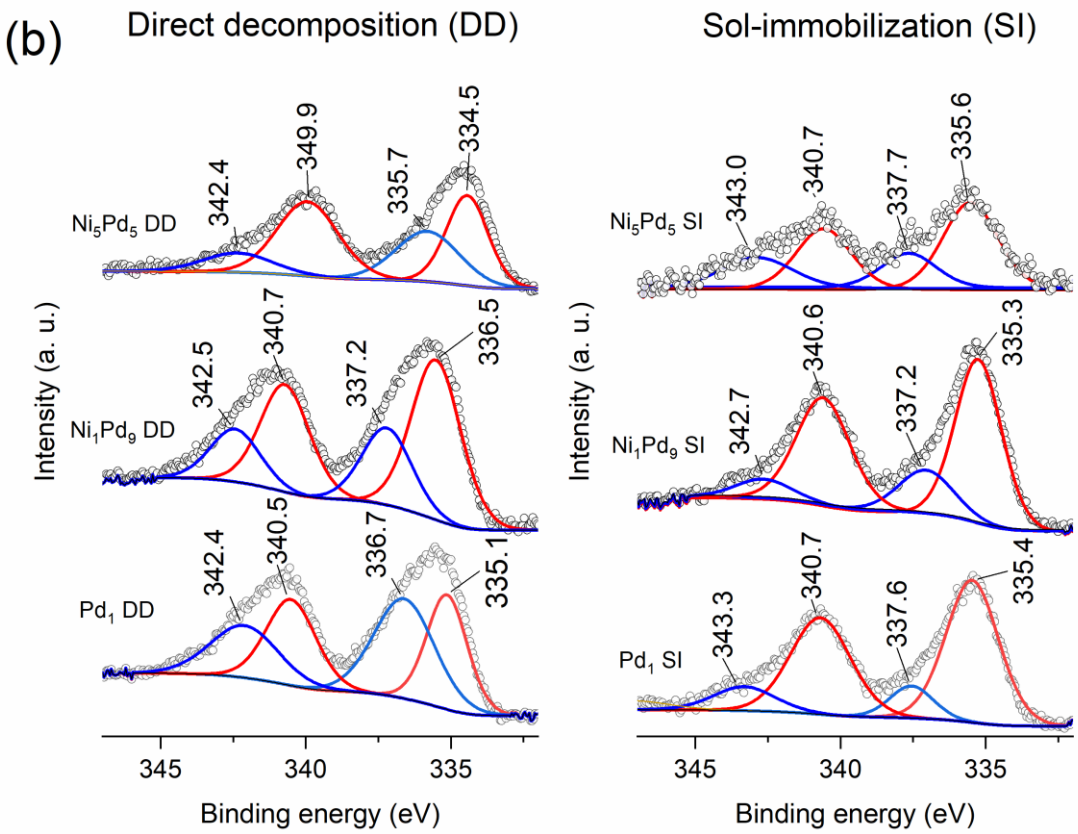

Figure S4: XPS spectra of the fresh Ni-Pd samples prepared from (a) Direct Decomposition, DD, and (b) Sol-Immobilization, SI.

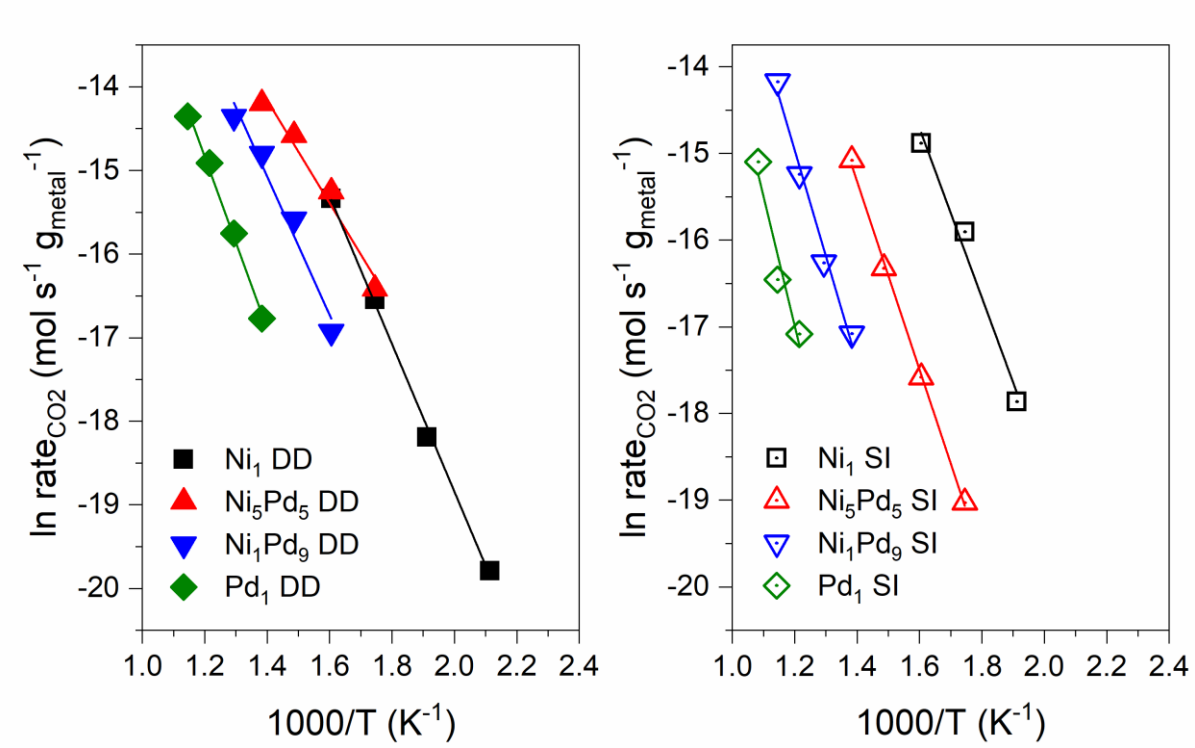

Figure S5: Arrhenius plot for RWGS in Ni-Pd/SiO_2 prepared following DD procedure (left) and SI procedure (right). Samples were pre-treated under H_2 at 400ºC for 30 min; W_{metal}=0.5 mg of total metal (Ni+Pd); 1 CO_2:4 H_2:45 Ar.